Surface-Wave Images of Western Canada: Lithospheric Variations Across the Cordillera/Craton Boundary

T. Zaporozan, Department of Geological Sciences, University of Manitoba, umzaporo@myumanitoba.ca

A.W. Frederiksen[1], Department of Geological Sciences, University of Manitoba, andrew.frederiksen@umanitoba.ca

A. Bryksin, Department of Geological Sciences, University of Manitoba, fater.gs@gmail.com

F. Darbyshire, Centre de recherche GEOTOP, Université du Québec à Montréal, darbyshire.fiona_ann@uqam.ca

Manuscript for *Canadian Journal of Earth Sciences*, revised for resubmission.

[1] Corresponding author. Full address: A.W. Frederiksen, Department of Geological Sciences, University of Manitoba, 125 Dysart Road, Winnipeg, MB, Canada, R3T 2N2. 204-474-9470

Abstract

Two-station surface-wave analysis was used to measure Rayleigh-wave phase velocities between 105 station pairs in western Canada, straddling the boundary between the tectonically active Cordillera and the adjacent stable craton. Major variations in phase velocity are seen across the boundary at periods from 15 to 200 s, periods primarily sensitive to upper-mantle structure. Tomographic inversion of these phase velocities was used to generate phase-velocity maps at these periods, indicating a sharp contrast between low-velocity Cordilleran upper mantle and high-velocity cratonic lithosphere. Depth inversion along selected transects indicates that the Cordillera/craton upper-mantle contact varies in dip along the deformation front, with cratonic lithosphere of the Taltson province overthrusting Cordilleran asthenosphere in the northern Cordillera, and Cordilleran asthenosphere overthrusting Wopmay lithosphere further south. Localized high-velocity features at sub-lithospheric depths beneath the Cordillera are interpreted as Farallon slab fragments, with the gap between these features indicating a slab window. A high-velocity feature in the lower lithosphere of the Slave province may be related to Proterozic or Archean subduction.

Keywords: Seismology, surface waves, tomography, Cordillera, craton

1. Introduction

The lithosphere beneath stable continental regions typically exhibits elevated seismic velocities to depths of 200 km or more, which has been attributed to a combination of low temperature and depleted composition (e.g. King 2005, Artemieva 2009, Aulbach 2012). By contrast, young orogenic belts are underlain by low-velocity upper mantle, attributed to a combination of high temperature, elevated volatile content, and a component of partial melt (see e.g. Hyndman et al. 2009). In North America, these two lithospheric regimes exist in close juxtaposition where the Phanerozoic Cordilleran Orogen abuts on Precambrian ancestral North America (Figure 1). Previous tomographic studies of North America (van der Lee and Nolet 1997a, Frederiksen et al. 2001, Bedle and Van der Lee 2009, Schaeffer and Lebedev 2014) image the Cordillera-craton transition as a major lithospheric velocity contrast, but questions remain regarding the sharpness of the transition, its orientation in three dimensions, and its relationship to crustal boundaries. We present a new study of the upper mantle beneath western Canada, based on two-station surface-wave analysis, that brings new constraints to bear on these questions.

East of the Cordillera, Western Canada is a Precambrian craton assemblage accreted in the Proterozoic from Archean and younger blocks (Whitmeyer and Karlstrom 2007). The Slave, Superior, Rae, Hearne, and Sask cratons are all of Archean age. These cratons assembled during the Proterozoic via the Taltson, Wopmay, and Trans-Hudson orogens. Their western boundary was a passive rifted margin in the Late Proterozoic (Gabrielse and Yorath 1991), onto which a series of terranes were accreted, beginning with the Intermontane Superterrane in the Jurassic (Clowes et al. 2005). This collision produced a fold-and-thrust belt extending to the current

Cordilleran deformation front. A later collision of the Insular Superterrane in the Cretaceous extended the Cordillera westward to its present extent.

2. Data and analysis

The Geological Survey of Canada (GSC) operates the Canadian National Seismograph Network (CNSN), which has been recording digital broadband data since the early 1990s (North and Basham 1993). Further instrumentation was installed as part of the Portable Observatories for Lithospheric Analysis and Research Investigating Seismicity (POLARIS) project (Eaton et al. 2005), the data from which is also archived by the GSC. We collected data from CNSN and POLARIS stations in western and central Canada, corresponding to earthquakes of magnitude greater than 6, at any distance from the receivers, whose propagation paths lay within 5° of the paths between selected station pairs (Figure 2). These pairs were selected to give consistent coverage of western Canada, and do not include all possible station pairs, particularly in western British Columbia where stations are more closely spaced than is appropriate for the intended resolution of this study. The downloaded data were inspected for Rayleigh-wave signal quality before use. The station responses were removed by conversion to displacement before further analysis; all stations used are broad-band, with all but two stations (ILKN and VGZ) having significant velocity response (at least 10% of the peak value) to periods of 200 s or longer. A plot of instrument responses is provided as supplemental material.

Two-station surface-wave analysis is a widely-used technique with a long history (beginning with Sato 1955) in which the change in waveform between two receiving stations is measured. Under the assumption that the waveform change is determined entirely by the structure along the great-circle path connecting the station pair, the waveform change may be used to isolate structure between the receiving instruments, even in aseismic regions. Thus, two-

station analysis is appropriate for Canada, which has limited seismic activity away from the west coast; previous studies have successfully applied this approach to the Canadian Arctic (Darbyshire 2005), Hudson Bay (Darbyshire and Eaton 2010), the Superior Province (Darbyshire et al. 2007), the southern Cordillera (Bao et al. 2014), and the northern Cordillera (McLellan et al. 2018).

Two-station analysis is generally applied at large distances from the earthquake source. Under these conditions, the different surface-wave modes are well separated and the fundamental Rayleigh mode dominates vertical-component recordings. A single mode's propagation may be described by a dispersion curve showing the relationship between frequency and velocity; the velocity considered may be either group velocity (velocity of energy transport, measured by determining the travel time of the signal envelope peak) or phase velocity (velocity of the phase of a single frequency, measured by determining the phase shift over a given distance). As the group velocity dispersion curve may be determined from the phase velocity, but not vice versa, the phase velocity contains more information (see e.g. Stein and Wysession 2003).

We measure phase-velocity dispersion curves using the cross-correlation technique of Meier et al. (2004); an example is given in Figure 3. Two vertical-component recordings of the same event, at stations that lie within 5° of a common great-circle path to the source, are cross-correlated. The phase of the cross-correlation corresponds to the phase difference between the two traces, with an ambiguity of $2\pi n$ radians, where n is an integer. For a cross-correlation phase of Φ measured between two stations separated by a distance x at angular frequency ω, the phase velocity will be

$$c(\omega) = \frac{x\omega}{\phi + 2\pi n}$$

and therefore multiple velocities are compatible with the measurement, the possible solutions being more closely spaced at higher frequencies. In practical use, the distance x is taken to be the difference between the source-receiver distances for each station, to avoid biased measurements for events not perfectly aligned with the two-station path. At sufficiently low frequency, there is likely to be only one phase-velocity value that falls within a realistic range; thus, the approach of Meier et al. (2004) is to begin at the longest period with significant coherent energy, and continue the dispersion curve to higher frequencies while assuming that the curve is smooth (as large jumps in phase velocity are unphysical). Multiple events were analysed for each station pair, incorporating paths travelling in both possible directions, and the resulting set of dispersion curves was averaged to obtain a single high-quality curve for each station pair. Two stages of quality control were performed: on individual paths, events were included in the average only in frequency bands that showed consistency with other events, and on the averaged curves, paths were edited to exclude frequency bands with strong deviations (more than 5%) from the average of all paths.

3. Results

3.1 Dispersion curves

Figure 4 shows the complete set of dispersion curves obtained in this study, after quality control was performed. A total of 105 curves was measured, at periods ranging from 16 to 333 s depending on path length and data quality; generally speaking, longer periods were measurable on longer paths and shorter periods on shorter paths. We do not, however, have high confidence in the longest periods, which are sparsely sampled, and therefore only periods up to 200 s are shown in the figure. The curves all show a velocity that increases with period, as would be expected given that longer periods sample greater depths. In the 40-200 second range, which is

most sensitive to lithospheric depths, the path-to-path variation covers a range of ≈ 400 m/s. This variation is systematic with path location, with eastern paths being faster and western paths being slower.

The spatial variation of phase velocities is more apparent in map view (Figure 5). At relatively short periods (up to 50 s), low velocities are clearly restricted to the Cordillera, while moderate to high velocities occur further east. At longer periods, more paths sampling both areas are present; though there is still a trend of velocity increasing eastward, there are also a number of crossing paths with distinctly different velocities. The true distribution of phase velocity cannot be determined without tomographic inversion.

3.2 Tomographic resolution and maps

Under the assumption that two-station measurements represent averages along great-circle paths, the recovery of 2-D dispersion maps is a linear inverse problem (Montagner 1986). We solved for a grid of phase velocities spaced 1° apart in latitude and 2° in longitude, with smoothing and damping constraints; the correct regularization level was determined by the L-curve method (Parker 1994). Each period was solved for independently, yielding maps from 30 to 160 s at 10 s intervals.

We performed lateral resolution tests using the path coverage for three relevant periods (50, 80, and 120 s; Figure 6). For an input model consisting of 4° (latitude) by 8° (longitude) blocks of alternating positive and negative 0.4 km/s velocity perturbations, we calculated average velocities for each path, added errors comparable to the scatter in the real data, and inverted using the same parameters as for the real data. The size of the blocks used reflects the feature size we are able to recover: ~ 450 km over most of the map area. The results indicate that the boundaries of features of this scale can be recovered accurately (within ~ 100 km) west of ~

100°W and south of 70°N, albeit with significant underestimation of anomaly magnitudes, and that resolution is best at moderate periods (60-100 s). Given that our regularization is smoothing-based, larger-scale features than this will be recovered more accurately.

Final dispersion maps for the real data set are shown in Figure 7. The Cordillera is low-velocity at all periods, with the edge of the low-velocity region corresponding closely to the Cordillera/craton boundary at periods of 80 s and less. At longer periods, the edge is more complex, with low velocities extending some distance into the craton north of 52°N. The Cordilleran low-velocity region is truncated north of 65°N at all periods; its southern and western boundaries are not imaged by this study.

East of the Cordillera, phase velocities are moderate to high (e.g. > 4.2 km/s at 80 s period). At short periods, resolution does not extend much east of 110°W due to a lack of high-frequency measurements along the longer paths in the eastern portion of the model. At periods of 80 s and higher, the highest phase velocities detected are at the eastern edge of the resolved region, ca. 95°W. Localized high-velocity zones are detected beneath Great Slave Lake (at the southern tip of the Slave Province) and along the southern edge of the model ca. 110°W.

3.3 Depth inversion and cross-sections

Rayleigh-wave period is often used as a depth proxy in surface-wave studies due to the increase in depth sensitivity with period; however, as any given velocity measurement is sensitive to a large range of depths, phase velocities must be inverted in order to constrain seismic velocity as a function of depth. The depth sensitivity of Rayleigh-wave phase velocities is model-dependent, requiring a nonlinear depth inversion.

We inverted for depth using the widely-used Computer Programs in Seismology package (Herrmann 2013), using phase velocities extracted from the tomographic maps, at periods

ranging from 30 to 160 s at 10 s intervals, the range of periods at which we are most confident in the map coverage. We used a starting model simplified from IASP91 (Kennett and Engdahl 1991), with fixed layer thicknesses ranging from 15 to 25 km (including a two-layer crust 35 km thick; see Figure 8), and inverted for S velocity over 5 iterations, with P velocity determined using a Poisson's ratio fixed to match the base model values (which range from 0.20 to 0.29), and density calculated from the P velocity. Smoothing regularization was used to compensate for the non-uniqueness of the inversion and to encourage model simplicity.

Synthetic tests of the depth inversion are shown in Figure 8. For each test, an input model containing a large (300 m/s) perturbation from IASP91 was used to generate a dispersion curve, using the same period sampling as the real data. The dispersion curve was then inverted (using the same inversion parameters as the real data) to test recovery of the input. We find that low-velocity features are significantly smeared, but not missed; high-velocity features at relatively shallow depth (above 150 km) are recovered, but produce a weaker low-velocity artefact below, while deep high-velocity anomalies are poorly recovered. These effects are a consequence of the non-linearity of surface-wave depth inversion, and will be less severe for weaker velocity perturbations.

To generate cross-sections, we spatially interpolated phase velocities at 50 km intervals from all dispersion maps, along five great-circle trajectories (Figure 9). The resulting dispersion curves were then inverted to form 1-D S velocity models, as described above; the 1-D models were concatenated to form a 2-D model along each transect. An example of this procedure is given in Figure 10, in which the series of dispersion curves is presented as a pseudosection (top panel) and inverted to obtain a velocity model (presented in both relative and absolute velocity terms). It is worth noting that the lack of short-period sampling in some areas affects the

194 inversion; northeast of the 1100 km point along the transect, the shortest periods are not available
195 (due to longer two-station paths in this region) and the shallowest part of the model is not well
196 constrained. As a consequence, northeast of 1100 km, velocity anomalies appear weaker due to
197 upward smearing of structure into the poorly-sampled shallow depth range. We therefore expect
198 that mantle velocity anomalies will be somewhat underestimated in the more poorly-
199 instrumented portions of the study area; this effect is most pronounced on the AA-AA' section
200 shown in Figure 10.

201 Transects were selected to examine the Cordillera-craton transition along three near
202 boundary-perpendicular sections (AA-AA', BB-BB' and CC-CC'), along-strike variation within
203 the Cordilleran low-velocity anomaly (DD-DD'), and a high-velocity feature detected near Great
204 Slave Lake in the dispersion maps (EE-EE'). The Cordillera is underlain by a low-velocity
205 feature (marked as A on the cross-sections; Figures 11 and 12) averaging 2-4% below IASP91
206 velocity down to ~250 km depth. The adjacent cratonic lithosphere (B) is underlain by high-
207 velocity lithosphere (5-8% above IASP91) down to 200-250 km depth; the contact between these
208 two anomalies is quite sharp (~ 8-10% over 200-300 lateral km at lithospheric depths), lies
209 directly beneath the crustal contact, and is not vertical. In the northern two cross-sections (CC-
210 CC' and BB-BB'; Figure 11) the contact dips 10-20° to the northeast, with cratonic lithosphere
211 overlying asthenospheric material associated with the Cordillera; by contrast, the southernmost
212 section (AA-AA') shows a dip of ~ 30° in the opposite direction. The depth extent of Cordilleran
213 low velocities varies somewhat along strike, shallowing to ~ 150 km depth beneath southern
214 British Columbia (DD-DD'; Figure 12). Our synthetic tests showed that high velocities at
215 lithospheric depths can produce low-velocity artefacts below; however, the artefacts are

significantly weaker than the high-velocity anomalies they underlie, which is not the case where feature A underlies feature B.

A localized high-velocity zone (feature C) centred on Great Slave Lake (62°N, 115°W) is visible on longer-period dispersion maps (Figure 7). The two cross-sections that intersect this zone (BB-BB' and EE-EE'; Figures 11 and 12) show a high-velocity feature from ≈ 125-275 km, extending somewhat deeper than is typical for cratonic lithosphere in North America (200-250 km; Eaton et al. 2009, Yuan et al. 2014). Even deeper high-velocity features (labelled D) are seen in patches beneath the Cordillera and adjacent areas.

4. Discussion

The Cordilleran mantle velocities we have measured are very low – for instance, at 400 km along the BB-BB' transect, the lowest mantle S velocity attained is 4.25 km/s from 155-170 km depth. Though a very low value for this depth (IASP91 reaches 4.51 km/s at 160 km), it is consistent with the models of Van der Lee and Frederiksen (2005) and Schaeffer and Lebedev (2014), which have comparable velocities in the same location. Based on the velocity-temperature calculations of Hyndman et al. (2009), this low velocity would correspond to a temperature of ~ 1200-1250°C, which is in accordance with previous studies, implying asthenospheric material underlying a weak, thin lithosphere and raising the possibility of small-scale convection in the Cordilleran upper mantle (Hyndman 2010).

Though our measurements of Cordilleran upper-mantle velocity primarily confirm earlier studies, this study provides novel high-resolution constraints on a significant portion of the Cordillera/craton boundary. Our cross-sections show that the mantle boundary is not vertical (Figure 11), with some high-velocity material extending west of the Cordilleran deformation

front in the crust. This may help to explain why some models place the boundary west of the front (see e.g. Frederiksen et al. 2001, McLellan et al. 2018).

Our most remarkable observation at the Cordillera/craton boundary is the change in dip direction from northeastern (cratonic material overthrusting Cordilleran asthenosphere) on the northern and central cross-sections (CC-CC' and BB-BB', Figure 11) to southwestern (Cordilleran asthenosphere overthrusting cratonic lithosphere) in the southernmost cross-section. This change, which was also detected in a recent North American model (Schaeffer et al. 2017), is seen in previous smaller-scale models. Surface and body-wave models of the southern Cordillera (Bao et al. 2014, Chen et al. 2017) show a steeply westward-dipping or vertical boundary, while models of the northern Cordillera show northeast dips (Cook and Erdmer 2005, Mercier et al. 2009). Models of the United States are not directly comparable due to the influence of the Yellowstone hotspot.

A possible explanation for the difference in dip direction at the lithospheric contact may be that the northern two cross-sections sample the Wopmay orogen, while the southernmost cross-section intersects the Taltson. Though both of these orogens were assembled through eastward-dipping subduction (McDonough et al. 2000, Davis et al. 2015), their western edges consist of different terranes (the Hottah for the Wopmay and the Buffalo Head for the Taltson). These terranes have different origins, and it is possible that their associated lithospheres are rheologically distinct. Edge-driven convection has been proposed for the southern Cordillera (Hardebol et al. 2012, Bao et al. 2014); modelling results indicate that mantle viscosity is an important control on the behaviour of the Cordillera/craton transition. It is thus plausible that a rheological difference between cratonic lithosphere of different affinity is affecting the shape of the mantle boundary, but further modelling is needed to support this.

Localized high-velocity features at sub-lithospheric depths (feature D; Figures 11 and 12) are found at various points beneath the Cordillera and craton. High velocities at these and greater depths appear in a number of tomographic models (see e.g. van der Lee and Nolet 1997b, Ren et al. 2007) and are commonly attributed to remnants of the subducted Farallon or Kula slab. The lateral resolution of our model does not permit an interpretation of the lateral extent of these features east of the Cordillera (as shown by the longest-period resolution test in Figure 6). However, as our path density is highest within the Cordillera itself, the discontinuous nature of feature D in section DD-DD' is probably a real feature, though ~ 350 km depth is at the limit of resolution for fundamental-mode Rayleigh waves.

Gaps in subducting slabs, resulting from processes such as ridge/trench contact, are known in the literature as slab windows. Slab windows have been proposed to exist north and south of the Juan de Fuca slab (Thorkelson and Taylor 1989); the southern window is seen in northern California (Hawley et al., 2016), while an additional slab gap is visible as a low-velocity feature beneath Oregon (Tian and Zhao 2012). We interpret feature D as slab remnants interrupted by a northern Cordilleran slab window, and therefore that the slab is absent from 400-1200 km along the DD-DD' cross-section. This range corresponds well with lateral velocity contrasts at ≈ 50°N and 60°N seen in the teleseismic P velocity model of Mercier et al. (2009).

The high-velocity feature labelled C in sections BB-BB' and EE-EE' cannot be attributed to recent subduction. Its depth of 150-250 km beneath the stable craton places it at the base of the lithosphere; its velocity of up to 10% over IASP91 is remarkable, indicating that it is fast even relative to the generally high-velocity surrounding cratonic lithosphere. A high-velocity feature beneath the Slave craton was previously found in this depth range using array analysis of surface waves (Chen et al. 2007), while strongly-layered lithosphere is visible in receiver

functions (Bostock 1998). LITHOPROBE reflection data across the Slave craton's eastern boundary show dipping reflectors attributed to Proterozoic and Archean subduction (Cook et al. 1999) which, when extrapolated eastward, correspond with receiver-function arrivals bracketing the depth of feature C. We therefore propose that feature C preserves these subduction remnants in the lower portion of the Slave lithosphere.

5. Conclusions

Through two-station analysis of surface-wave records, we have mapped Rayleigh phase velocity across western Canada. The most salient feature of our dispersion maps is the sharp contrast between low-velocity Cordilleran upper mantle and high-velocity cratonic lithosphere. By extracting dispersion curves from the tomographic maps and inverting for S velocity structure, we have generated cross-sections examining the Cordillera/craton mantle boundary and surrounding region; these cross-sections show a change in dip of the mantle contact from northeast in the northern Cordillera to southwest in the southern Cordillera, which may reflect differences in rheology between the Wopmay and Taltson shield provinces. Isolated high-velocity features seen beneath the Cordilleran upper mantle may represent Farallon slab fragments, separated by a gap resulting from a Cordilleran slab window. A high-velocity feature at the base of the Slave Province lithosphere correlates with a previously interpreted Proterozoic subduction feature.

The main limitation on these results is the lack of resolution east of the Cordillera due to a limited station network. New instruments currently deployed in the Northern Cordillera (Ma and Audet 2017) will allow improvement of these images in the future, as will incorporation of instrumentation in the United States.

Acknowledgements

Funding for this research was provided by NSERC, the Geological Survey of Canada, and de Beers Canada. Pascal Audet and Ian Ferguson provided essential feedback on the M.Sc. thesis from which this paper is derived; thanks also to Andrew Schaeffer for helpful discussion. Thanks to Derek Schutt and an anonymous reviewer for reviews that significantly improved this manuscript.

References

Artemieva, I.M. 2009. The continental lithosphere: Reconciling thermal, seismic, and petrologic data. Lithos **109**(1-2): 23–46. doi:10.1016/j.lithos.2008.09.015.

Aulbach, S. 2012. Craton nucleation and formation of thick lithospheric roots. Lithos **149**(C): 16–30. Elsevier B.V. doi:10.1016/j.lithos.2012.02.011.

Bao, X., Eaton, D.W., and Guest, B. 2014. Plateau uplift in western Canada caused by lithospheric delamination along a craton edge. Nature Geoscience **7**(11): 830–833. doi:10.1038/ngeo2270.

Bedle, H., and Van Der Lee, S. 2009. S velocity variations beneath North America. J Geophys Res-Sol Ea **114**: –. doi:10.1029/2008JB005949.

Bostock, M.G. 1998. Mantle stratigraphy and evolution of the Slave province. J. Geophys. Res **103**: 21183–21200.

Chen, C.-W., Rondenay, S., Weeraratne, D.S., and Snyder, D.B. 2007. New constraints on the upper mantle structure of the Slave craton from Rayleigh wave inversion. Geophys Res Lett **34**: –. doi:10.1029/2007GL029535.

Chen, Y., Gu, Y.J., and Hung, S.-H. 2017. Finite-frequency P-wave tomography of the Western Canada Sedimentary Basin: Implications for the lithospheric evolution in Western Laurentia. Tectonophysics **698**(C): 79–90. Elsevier B.V. doi:10.1016/j.tecto.2017.01.006.

Clowes, R., Hammer, P.T., Fernández-Viejo, G., and Welford, J. 2005. Lithospheric structure in northwestern Canada from Lithoprobe seismic refraction and related studies: a synthesis. Can J Earth Sci **42**(6): 1277–1294.

Cook, F.A., and Erdmer, P. 2005. An 1800 km cross section of the lithosphere through the northwestern North American plate: lessons from 4.0 billion years of Earth's history. Can J Earth Sci **42**: 1295–1311. doi:10.1139/e04-106.

Cook, F.A., Velden, A.J., Hall, K.W., and Roberts, B.J. 1999. Frozen subduction in Canada's Northwest Territories: Lithoprobe deep lithospheric reflection profiling of the western Canadian Shield. Tectonics **18**(1): 1–24. doi:10.1029/1998TC900016.

Darbyshire, F.A. 2005. Upper mantle structure of Arctic Canada from Rayleigh wave dispersion. Tectonophysics **405**(1-4): 1–23. doi:10.1016/j.tecto.2005.02.013.

Darbyshire, F.A., and Eaton, D.W. 2010. The lithospheric root beneath Hudson Bay, Canada from Rayleigh wave dispersion No clear seismological distinction between Archean and Proterozoic mantle. Lithos **120**: 144–159. doi:10.1016/j.lithos.2010.04.010.

Darbyshire, F.A., Eaton, D.W., Frederiksen, A., and Ertolahti, L. 2007. New insights into the lithosphere beneath the Superior Province from Rayleigh wave dispersion and receiver function analysis. Geophys J Int **169**: 1043–1068. doi:10.1111/j.1365-246X.2006.03259.x.

Davis, W.J., Ootes, L., Newton, L., Jackson, V., and Stern, R.A. 2015. Characterization of the Paleoproterozoic Hottah terrane, Wopmay Orogen using multi-isotopic (U-Pb, Hf and O) detrital zircon analyses: An evaluation of linkages to northwest Laurentian Paleoproterozoic domains. Precambrian Research **269**: 296–310. Elsevier B.V. doi:10.1016/j.precamres.2015.08.012.

Eaton, D.W., Adams, J., Asudeh, I., Atkinson, G.M., Bostock, M.G., Cassidy, J.F., Ferguson, I.J., Samson, C., Snyder, D.B., Tiampo, K.F., and Unsworth, M.J. 2005. Investigating Canada's lithosphere and earthquake hazards with portable arrays. Eos **86**(17): 169–171. doi:10.1029/2005EO170001/full.

Eaton, D.W., Darbyshire, F.A., Evans, R.L., Grütter, H., Jones, A.G., and Yuan, X. 2009. The

358 elusive lithosphere–asthenosphere boundary (LAB) beneath cratons. Lithos **109**(1-2): 1–22.
359 doi:10.1016/j.lithos.2008.05.009.
360 Frederiksen, A., Bostock, M.G., and Cassidy, J.F. 2001. S-wave velocity structure of the
361 Canadian upper mantle. **124**: 175–191.
362 Gabrielse, H., and Yorath, C.J. 1991. Tectonic Synthesis. *In* Geology of the Cordilleran Orogen
363 in Canada. *Edited by* H. Gabrielse and C.J. Yorath. Accents Publications Service. pp. 677–
364 705.
365 Hardebol, N.J., Pysklywec, R.N., and Stephenson, R. 2012. Small-scale convection at a
366 continental back-arc to craton transition: Application to the southern Canadian Cordillera.
367 Journal of Geophysical Research: Solid Earth (1978–2012) **117**(B1).
368 doi:10.1029/2011JB008431.
369 Hawley, W.B., Allen, R.M., and Richards, M.A. 2016. Tomography reveals buoyant
370 asthenosphere accumulating beneath the Juan de Fuca plate. Science **353**(6306): 1406–1408.
371 American Association for the Advancement of Science. doi:10.1126/science.aad8104.
372 Herrmann, R.B. 2013. Computer Programs in Seismology: An Evolving Tool for Instruction and
373 Research. Seismological Research Letters **84**(6): 1081–1088. GeoScienceWorld.
374 doi:10.1785/0220110096.
375 Hyndman, R. 2010. The consequences of Canadian Cordillera thermal regime in recent tectonics
376 and elevation: a review. Can J Earth Sci **47**(5): 621–632.
377 Hyndman, R.D., Currie, C.A., Mazzotti, S., and Frederiksen, A. 2009. Temperature control of
378 continental lithosphere elastic thickness, Te vs Vs. Earth and Planetary Science Letters **277**:
379 539–548. doi:10.1016/j.epsl.2008.11.023.
380 Kennett, B.L.N., and Engdahl, E.R. 1991. Traveltimes for global earthquake location and phase
381 identification. Geophysical Journal of the Royal Astronomical Society **105**(2): 429–465.
382 Blackwell Publishing Ltd. doi:10.1111/j.1365-246X.1991.tb06724.x.
383 King, S.D. 2005. Archean cratons and mantle dynamics. Earth and Planetary Science Letters
384 **234**(1-2): 1–14. doi:10.1016/j.epsl.2005.03.007.
385 Ma, S., and Audet, P. 2017. Seismic velocity model of the crust in the northern Canadian
386 Cordillera from Rayleigh wave dispersion data. **54**(2): 163–172. doi:10.1139/cjes-2016-
387 0115.
388 McDonough, M.R., McNicoll, V.J., Schetselaar, E.M., and Grover, T.W. 2000.
389 Geochronological and kinematic constraints on crustal shortening and escape in a two-sided
390 oblique-slip collisional and magmatic orogen, Paleoproterozoic Taltson magmatic zone,
391 northeastern Alberta. Can J Earth Sci **37**: 1549–1573.
392 McLellan, M., Schaeffer, A.J., and Audet, P. 2018. Structure and fabric of the crust and
393 uppermost mantle in the northern Canadian Cordillera from Rayleigh-wave tomography.
394 Tectonophysics **724-725**: 28–41. Elsevier. doi:10.1016/j.tecto.2018.01.011.
395 Meier, T., Dietrich, K., Stöckhert, B., and Harjes, H.-P. 2004. One-dimensional models of shear
396 wave velocity for the eastern Mediterranean obtained from the inversion of Rayleigh wave
397 phase velocities and tectonic implications. Geophys J Int **156**(1): 45–58. doi:10.1111/j.1365-
398 246X.2004.02121.x.
399 Mercier, J.P., Bostock, M.G., Cassidy, J.F., Dueker, K., Gaherty, J.B., Garnero, E.J., Revenaugh,
400 J., and Zandt, G. 2009. Body-wave tomography of western Canada. Tectonophysics **475**(3-
401 4): 480–492. doi:10.1016/j.tecto.2009.05.030.
402 Montagner, J.P. 1986. Regional three-dimensional structures using long-period surface waves.
403 Ann Geophys.

404 North, R.G., and Basham, P.W. 1993. Modernization of the Canadian National Seismograph
405 Network. Seismological Research Letters **64**: 41. Seis. Res. Let.
406 Parker, R.L. 1994. Geophysical Inverse Theory. Princeton University Press.
407 Ren, Y., Stutzmann, E., van der Hilst, R., and Besse, J. 2007. Understanding seismic
408 heterogeneities in the lower mantle beneath the Americas from seismic tomography and
409 plate tectonic history. J. Geophys. Res **112**: 302.
410 Sato, Y. 1955. Analysis of Dispersed Surface Waves by means of Fourier Transform I. Bull.
411 Earthquake Res. Tokyo Univ. **33**: 33–47.
412 Schaeffer, A., and Lebedev, S. 2014. Imaging the North American continent using waveform
413 inversion of global and USArray data. Earth and Planetary Science Letters **402**(C): 26–41.
414 Elsevier B.V. doi:10.1016/j.epsl.2014.05.014.
415 Schaeffer, A.J., Audet, P., Mallyon, D., Currie, C.A., and Gu, Y.J. 2017. Transient tectonic
416 transition from Canadian Cordillera to stable shield?
417 . pp. 1–1.
418 Stein, S., and Wysession, M. 2003. An Introduction to Seismology, Earthquakes, and Earth
419 Structure. John Wiley & Sons.
420 Thorkelson, D.J., and Taylor, R.P. 1989. Cordilleran slab windows. Geol **17**(9): 833–836.
421 GeoScienceWorld. doi:10.1130/0091-7613(1989)017<0833:CSW>2.3.CO;2.
422 Tian, Y., and Zhao, D. 2012. P-wave tomography of the western United States: Insight into the
423 Yellowstone hotspot and the Juan de Fuca slab. Physics of the Earth and Planetary Interiors
424 **200-201**: 72–84. Elsevier. doi:10.1016/j.pepi.2012.04.004.
425 van der Lee, S., and Frederiksen, A. 2005. Surface wave tomography applied to the north
426 american upper mantle. Geophysical monograph.
427 van der Lee, S., and Nolet, G. 1997a. Upper mantle S velocity structure of North America. J.
428 Geophys. Res **102**(B10): 22815–22838.
429 van der Lee, S., and Nolet, G. 1997b. Seismic image of the subducted trailing fragments of the
430 Farallon plate. **386**(6622): 266–269.
431 Whitmeyer, S., and Karlstrom, K. 2007. Tectonic model for the Proterozoic growth of North
432 America. Geosphere **3**(4): 220.
433 Yuan, H., French, S., Cupillard, P., and Romanowicz, B. 2014. Lithospheric expression of
434 geological units in central and eastern North America from full waveform tomography. Earth
435 and Planetary Science Letters **402**(C): 176–186. Elsevier B.V.
436 doi:10.1016/j.epsl.2013.11.057.
437

Figures

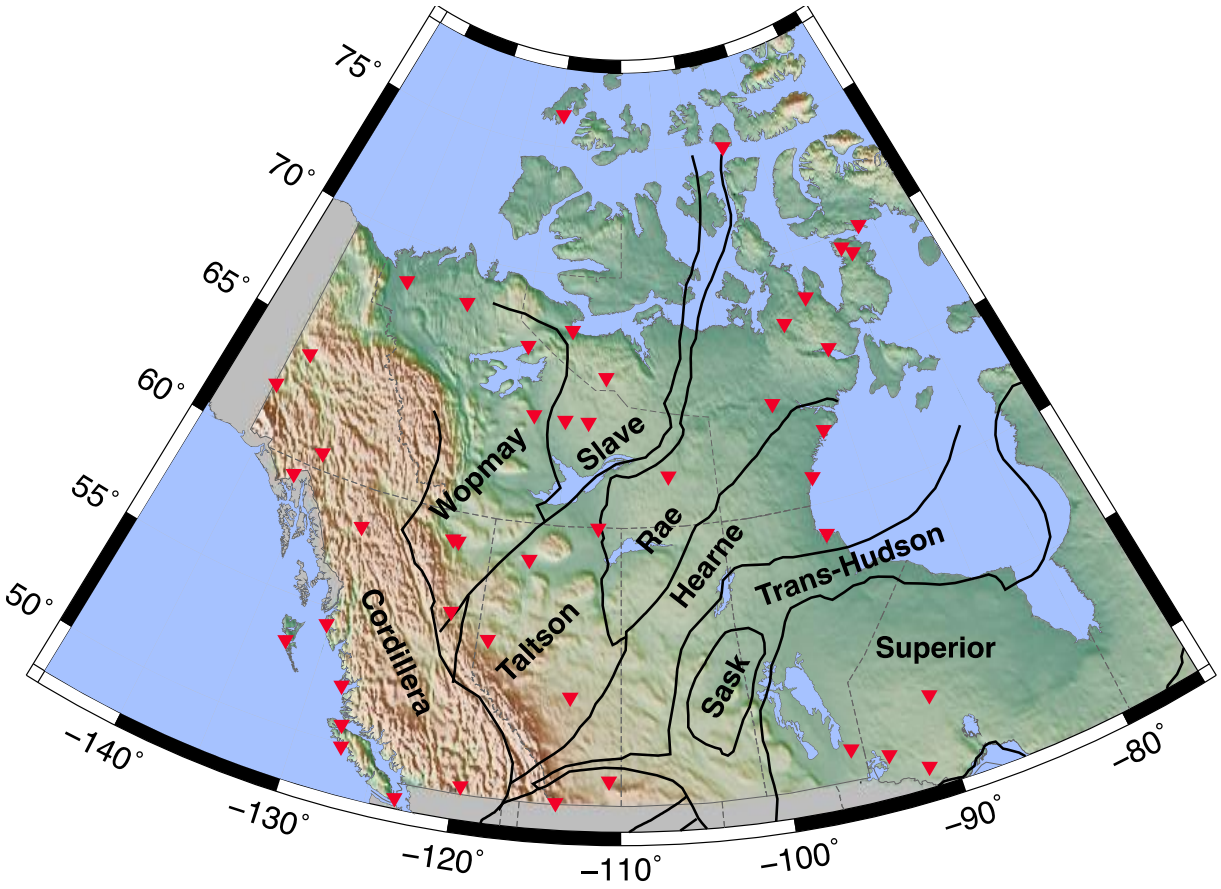

Figure 1: Seismic stations used in this study (red triangles), overlain on topography. Black lines indicate major tectonic boundaries (simplified from Whitmeyer and Karlstrom, 2007). Map projection: Lambert conic centred at 63°N, 110°W with standard parallels at 53°N and 73°N; the same projection is used for all other maps in this paper.

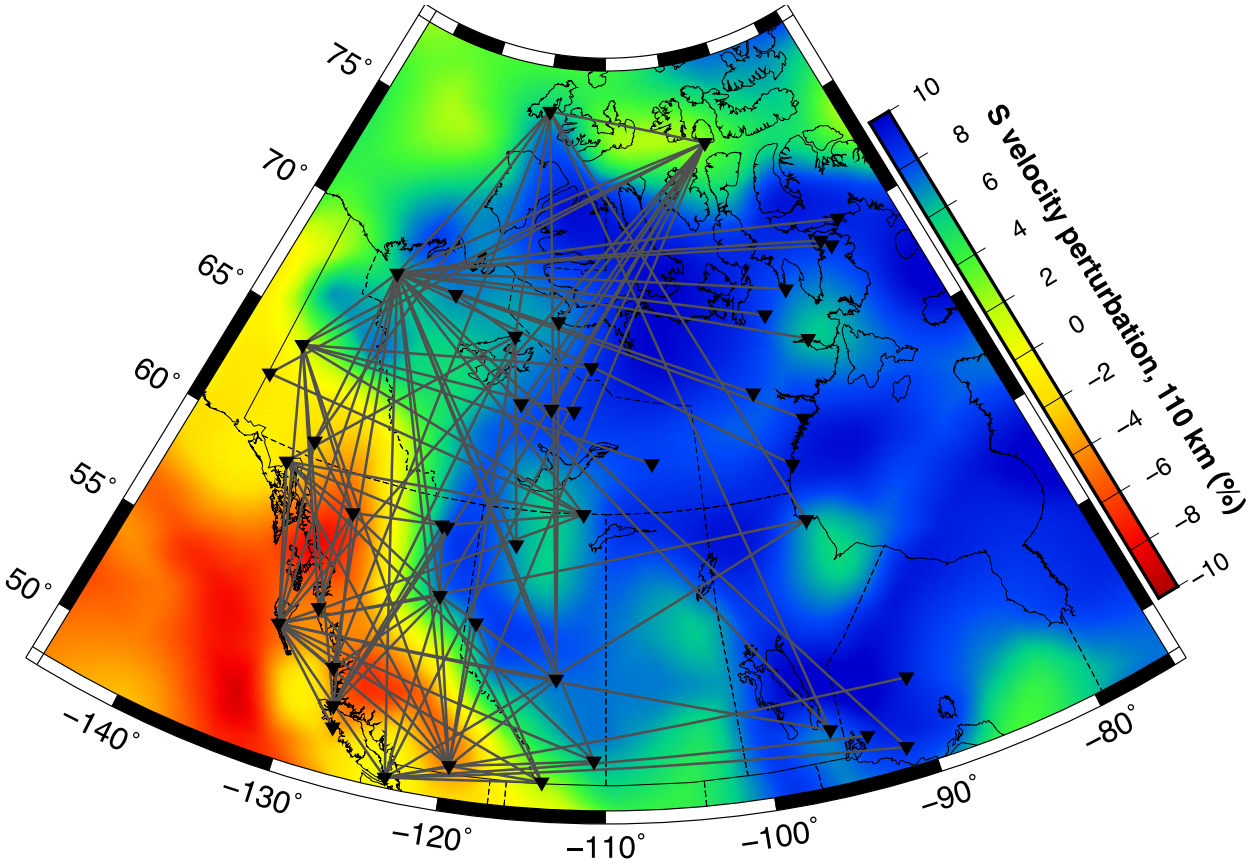

Figure 2: Two-station paths (grey lines) analyzed in this study. Background is seismic *S* velocity at 110 km depth, from the tomographic model of Schaeffer and Lebedev (2014).

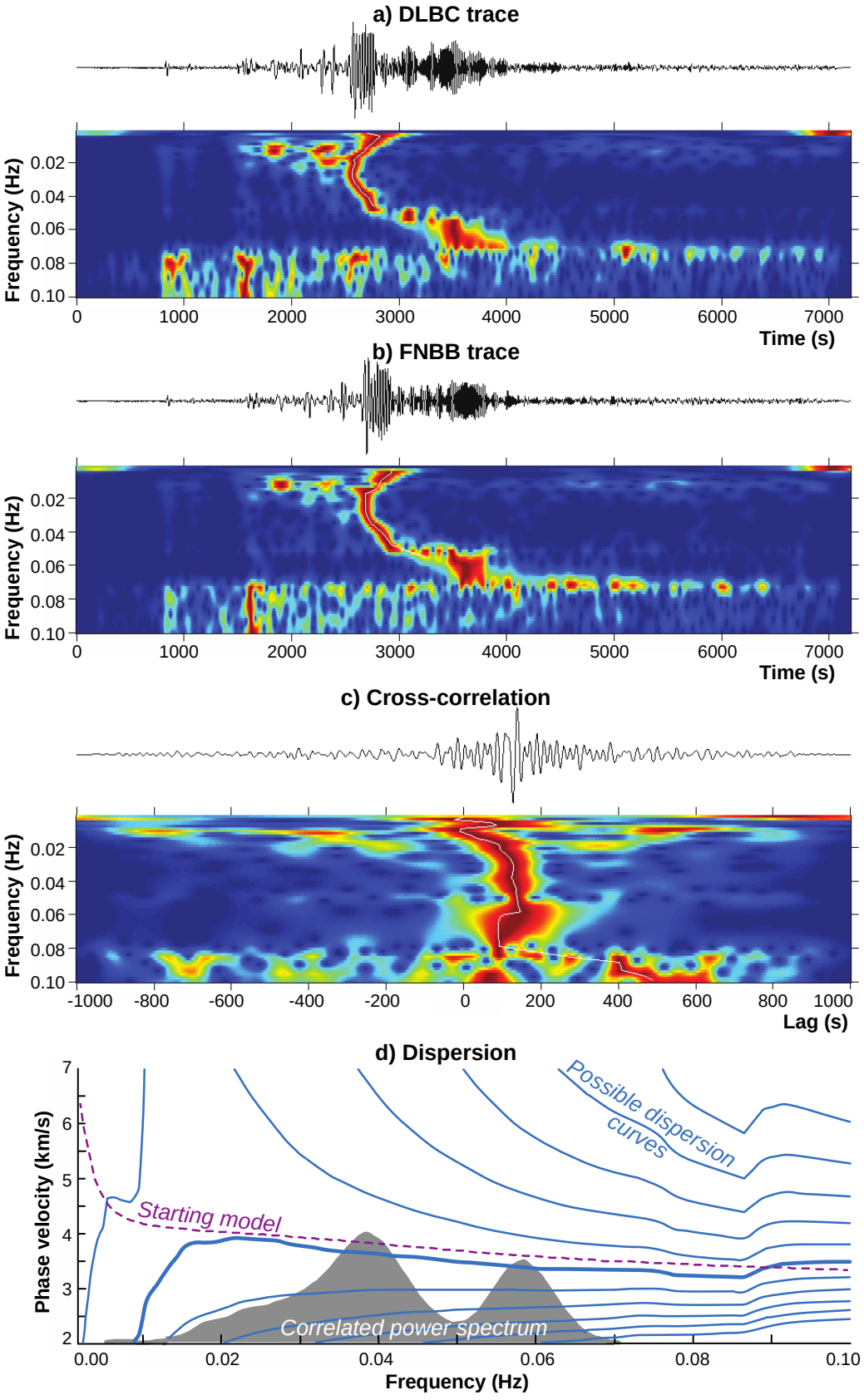
a) DLBC trace
Frequency (Hz)
0.02
0.04
0.06
0.08
0.10
0
1000
2000
3000
4000
5000
6000
7000
Time (s)
b) FNBB trace
Frequency (Hz)
Time (s)
c) Cross-correlation
Frequency (Hz)
-1000
-800
-600
-400
-200
0
200
400
600
800
1000
Lag (s)
d) Dispersion
Phase velocity (km/s)
Possible dispersion curves
Starting model
Correlated power spectrum
Frequency (Hz)

447

Figure 3: Two-station analysis for an event recorded at DLBC (Dees Lake, British Columbia) and FNBB (Fort Nelson, British Columbia). Individual traces (a, b) are shown along with a time-frequency analysis; the thin white line indicates group arrival time. The two traces are cross-correlated (c) and the cross-correlation phase determines possible Rayleigh phase-velocity curves (d, blue lines). Due to the $2n\pi$-radian ambiguity of phase, curves are closely spaced at high frequencies; at lower frequencies, only one is plausible (thick line) and may be followed to higher frequency. Here, the curve is usable from ≈ 0.02 to 0.07 Hz.

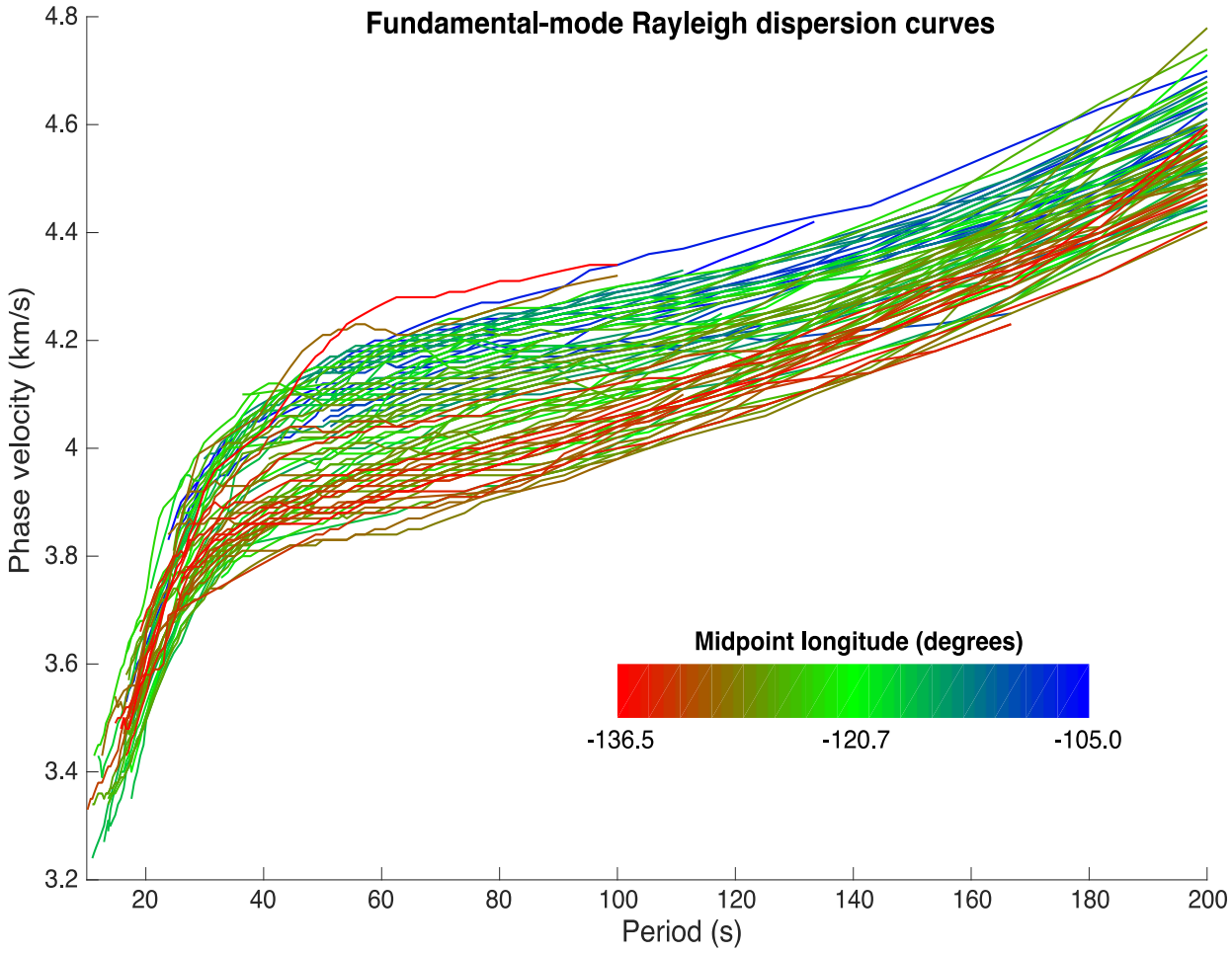

Figure 4: Average phase-velocity dispersion curves for all paths examined in this study. The curves are coloured based on the midpoint longitudes of the corresponding two-station paths.

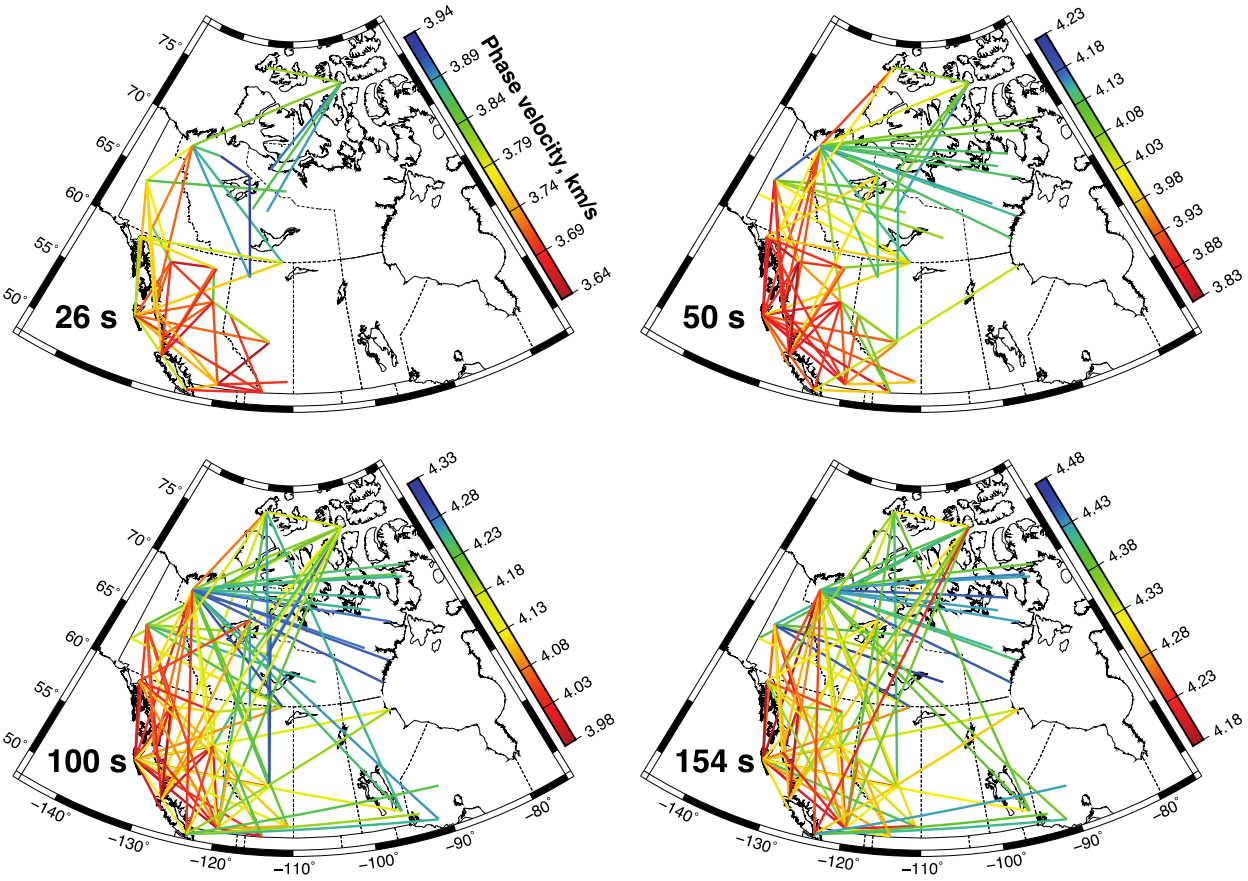

Figure 5: Phase velocities at four representative periods, plotted as shaded lines along the corresponding two-station great-circle paths. Note that the colour scale differs between panels.

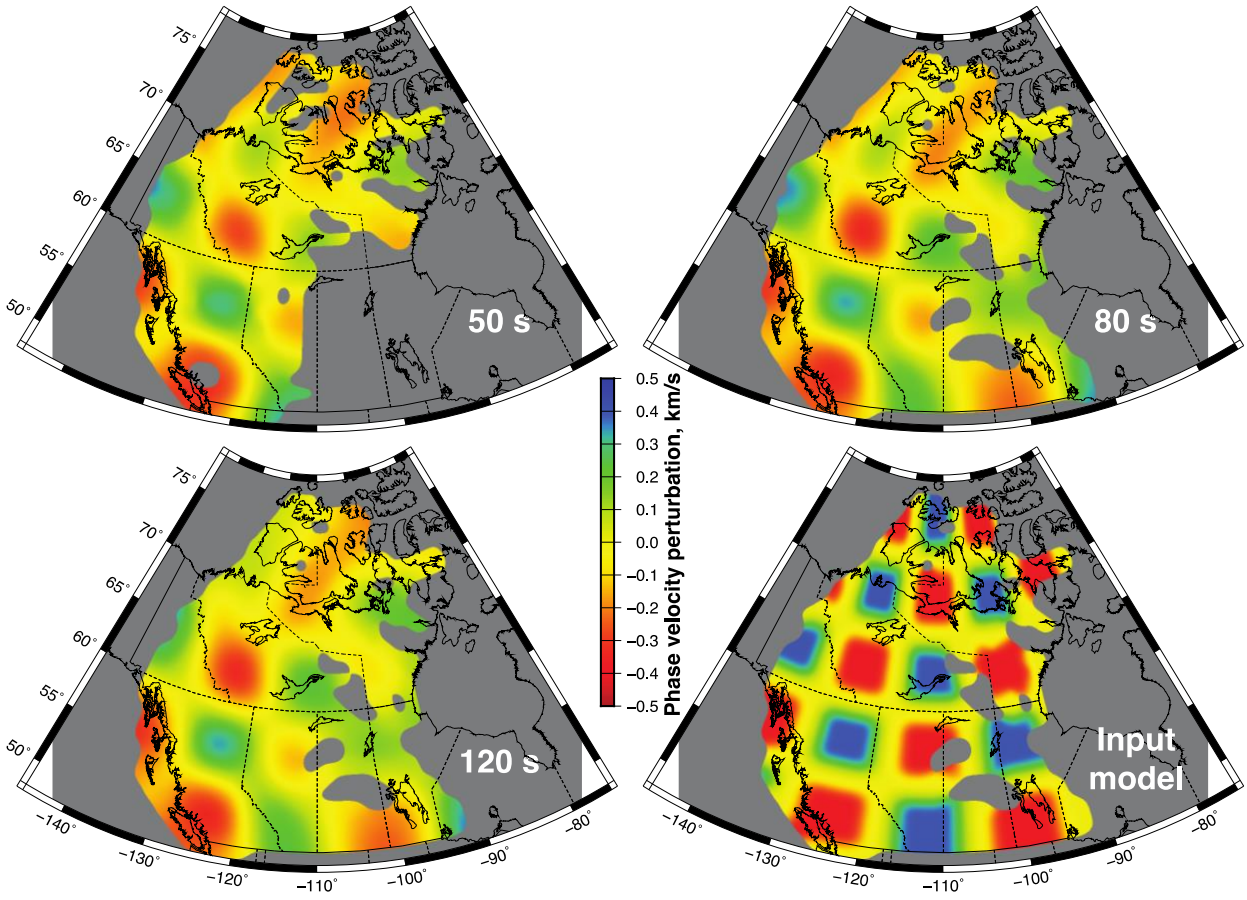

Figure 6: Checkerboard resolution tests for phase-velocity tomography, at three representative periods. Greyed-out model cells were not sampled by rays. The colour scale is the same for all plots.

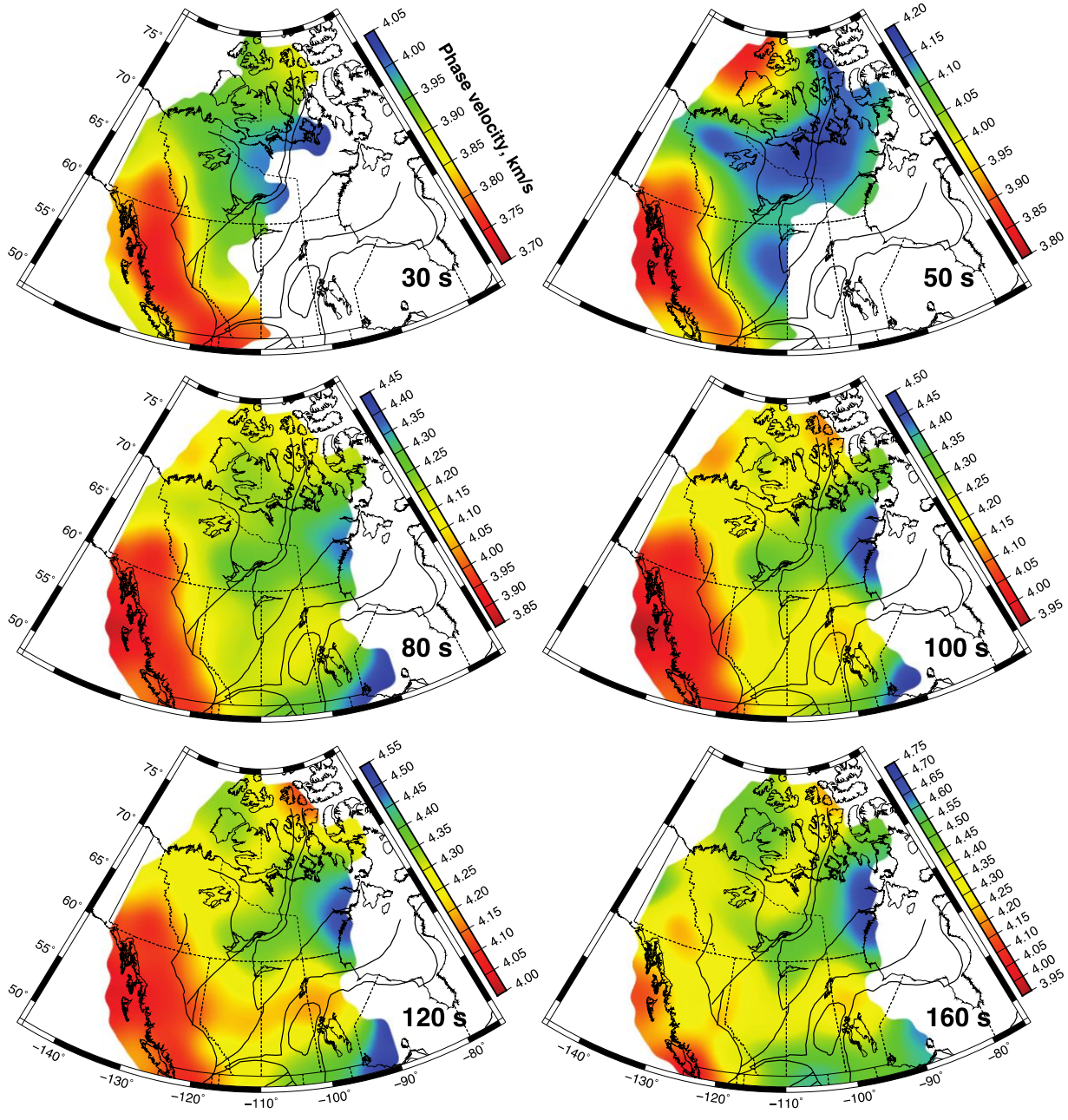

Figure 7: Recovered Rayleigh phase-velocity maps at six periods. The colour scale varies between plots. Black lines are tectonic boundaries from Figure 1.

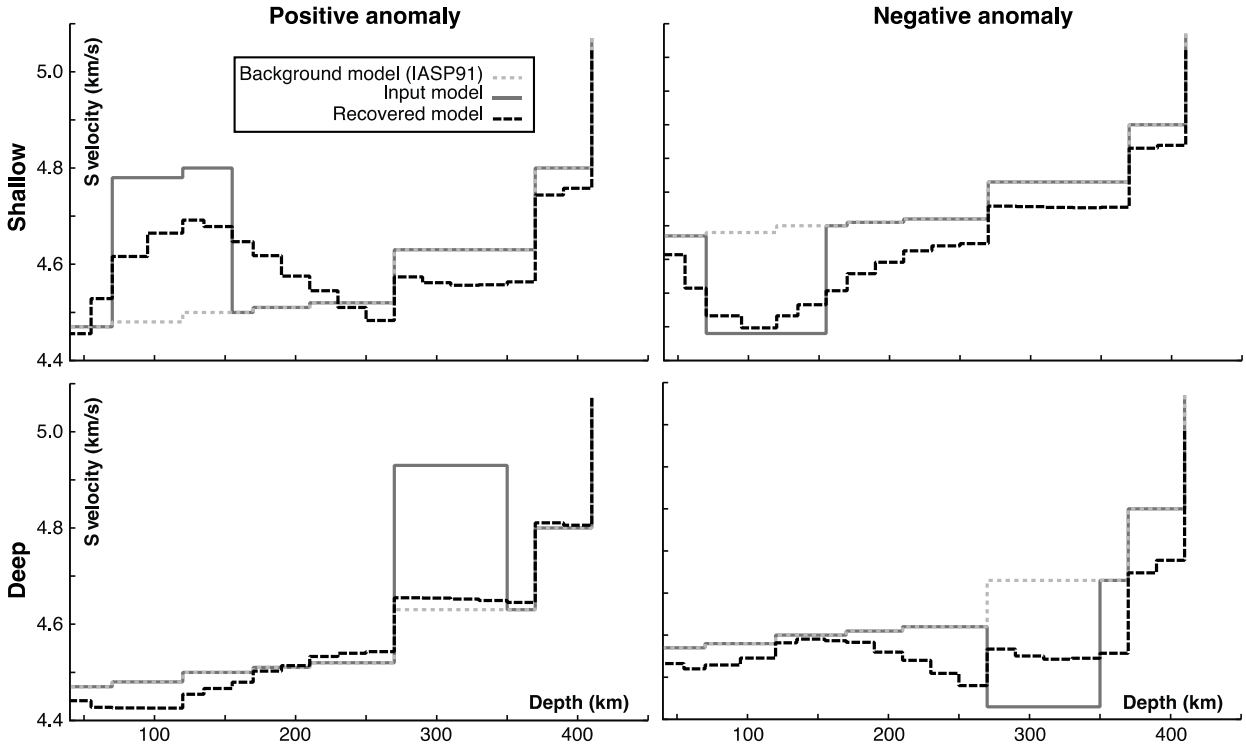

Figure 8: Synthetic tests of depth resolution. The input model (solid grey) contains a perturbation from the background (grey dotted); the recovered model (black dashed) is the result of generating synthetic data from the input model, then inverting the result.

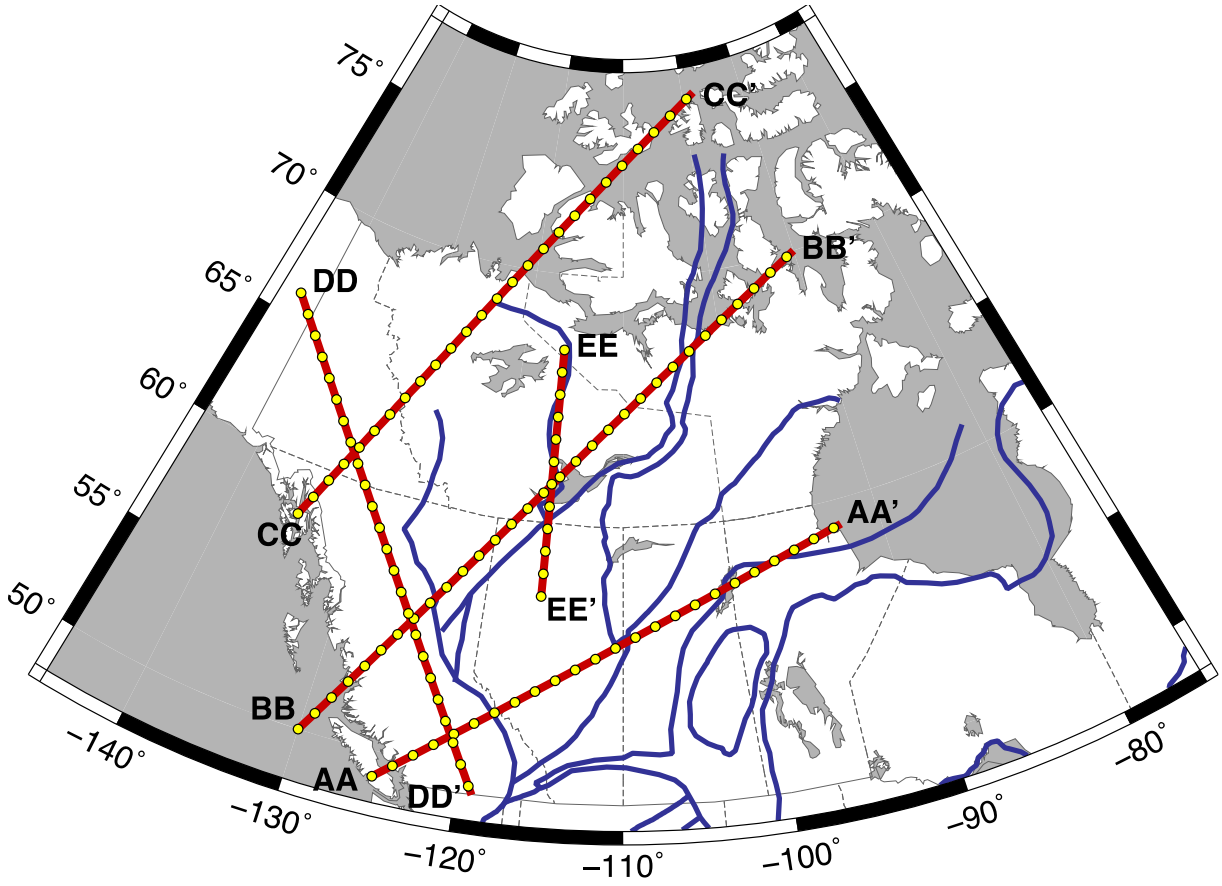

Figure 9: Locations of transects (red lines) inverted to form cross-sections. Yellow dots mark 100 km intervals. The blue lines are tectonic boundaries from Figure 1.

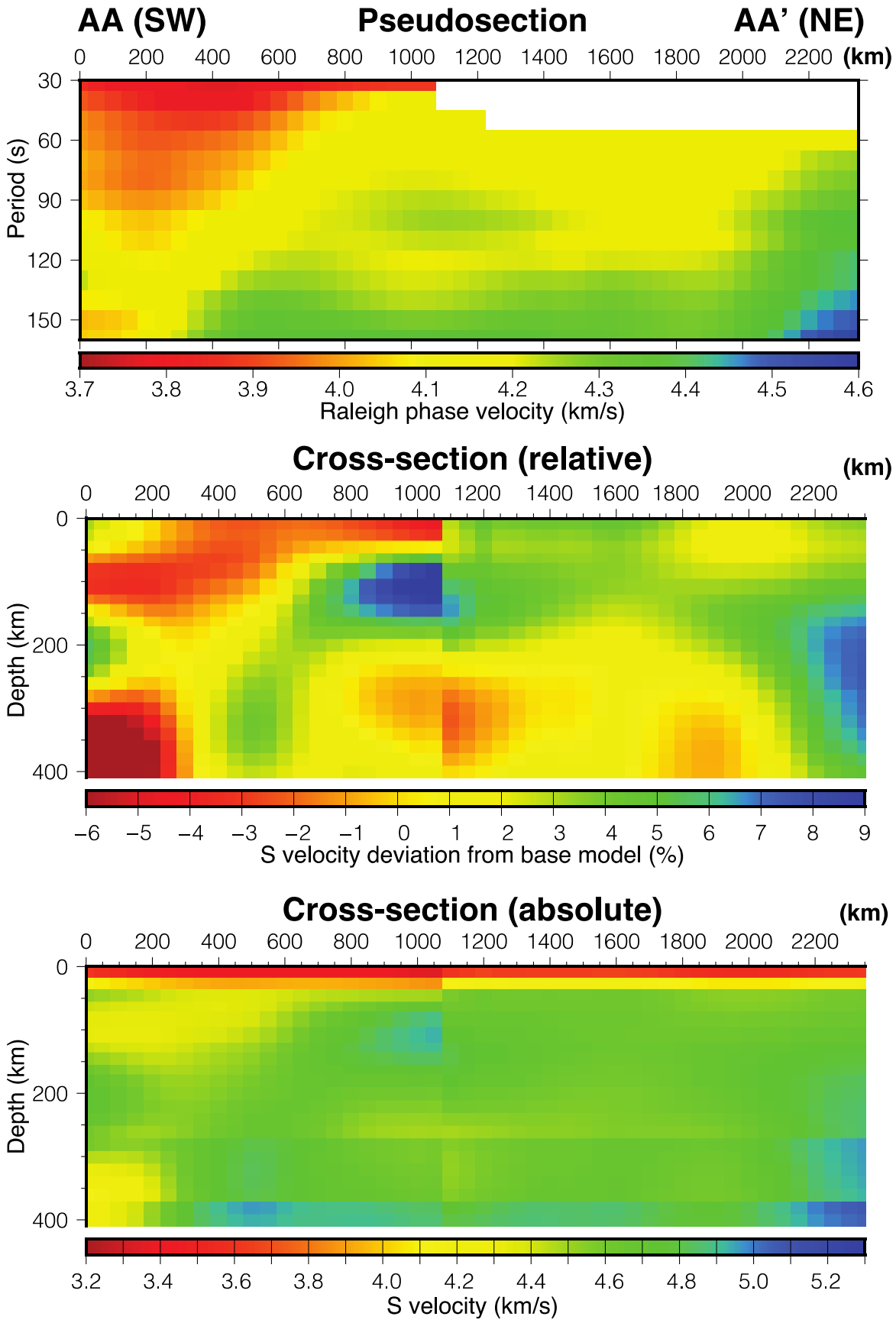
AA (SW)
Pseudosection
AA' (NE)
0 200 400 600 800 1000 1200 1400 1600 1800 2000 2200 (km)
Period (s)
30 60 90 120 150
3.7 3.8 3.9 4.0 4.1 4.2 4.3 4.4 4.5 4.6
Raleigh phase velocity (km/s)
Cross-section (relative)
(km)
0 200 400 600 800 1000 1200 1400 1600 1800 2000 2200
Depth (km)
0 200 400
−6 −5 −4 −3 −2 −1 0 1 2 3 4 5 6 7 8 9
S velocity deviation from base model (%)
Cross-section (absolute)
(km)
0 200 400 600 800 1000 1200 1400 1600 1800 2000 2200
Depth (km)
0 200 400
3.2 3.4 3.6 3.8 4.0 4.2 4.4 4.6 4.8 5.0 5.2
S velocity (km/s)

475

Figure 10: Example of the cross-section generation process for transect AA-AA'. A pseudosection (top) is extracted from dispersion maps, then each column is inverted separately to form a 1-D model. Concatenation of these 1-D models generates a cross-section, presented in terms of relative (middle) or absolute (bottom) velocity; the base model is IASP91.

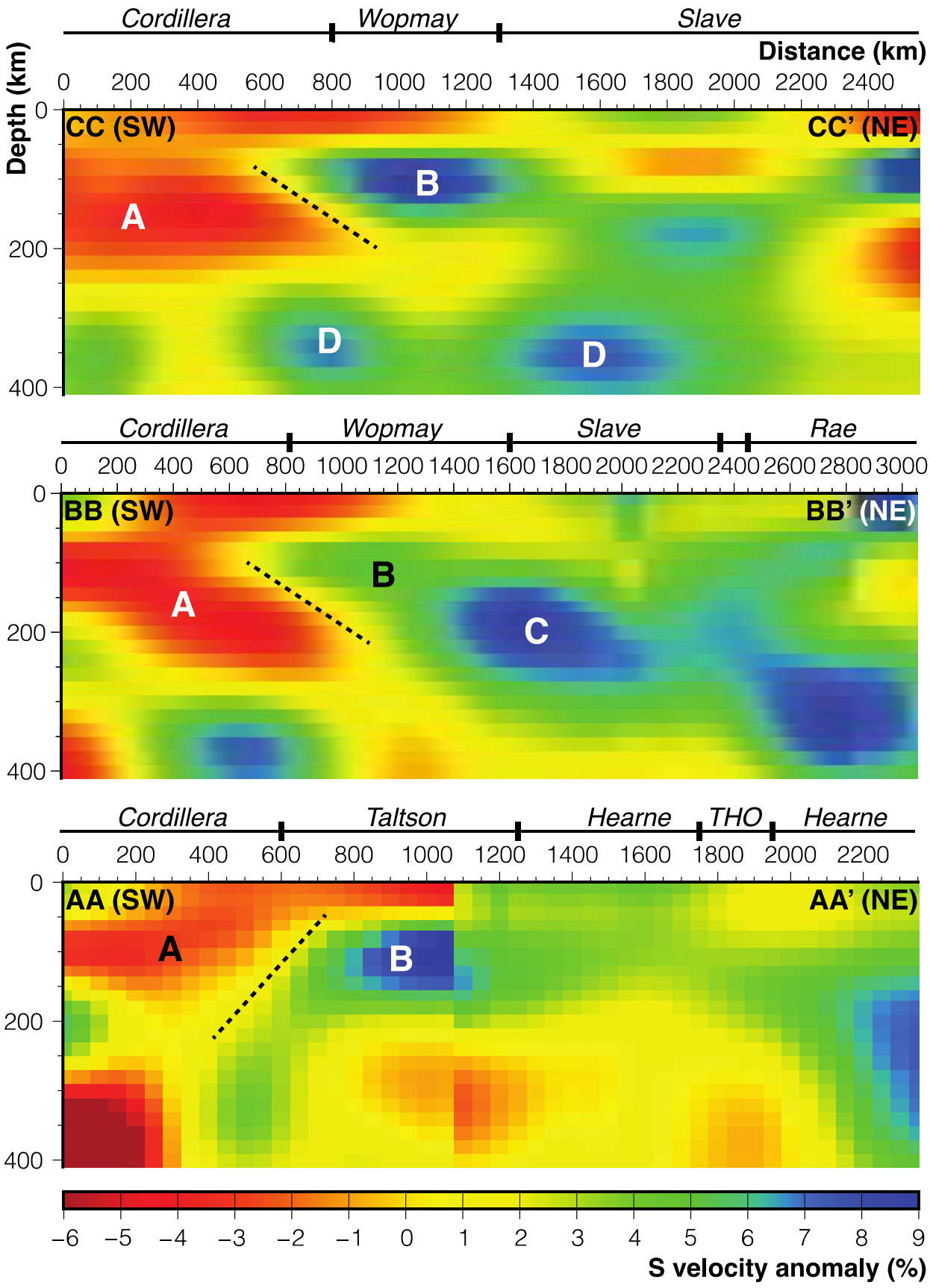
Cordillera
Wopmay
Slave
Distance (km)
0 200 400 600 800 1000 1200 1400 1600 1800 2000 2200 2400
Depth (km)
0
200
400
CC (SW)
CC' (NE)
A
B
D
D
Cordillera
Wopmay
Slave
Rae
0 200 400 600 800 1000 1200 1400 1600 1800 2000 2200 2400 2600 2800 3000
0
200
400
BB (SW)
BB' (NE)
A
B
C
Cordillera
Taltson
Hearne
THO
Hearne
0 200 400 600 800 1000 1200 1400 1600 1800 2000 2200
0
200
400
AA (SW)
AA' (NE)
A
B
−6 −5 −4 −3 −2 −1 0 1 2 3 4 5 6 7 8 9
S velocity anomaly (%)

480

Figure 11: Three relative-velocity cross-sections perpendicular to the Cordillera-craton boundary, ordered from north to south. Labels at the top of each indicate the tectonic provinces sampled. Letters indicate features discussed in text; dashed line indicates approximate 0% contour between features A and B.

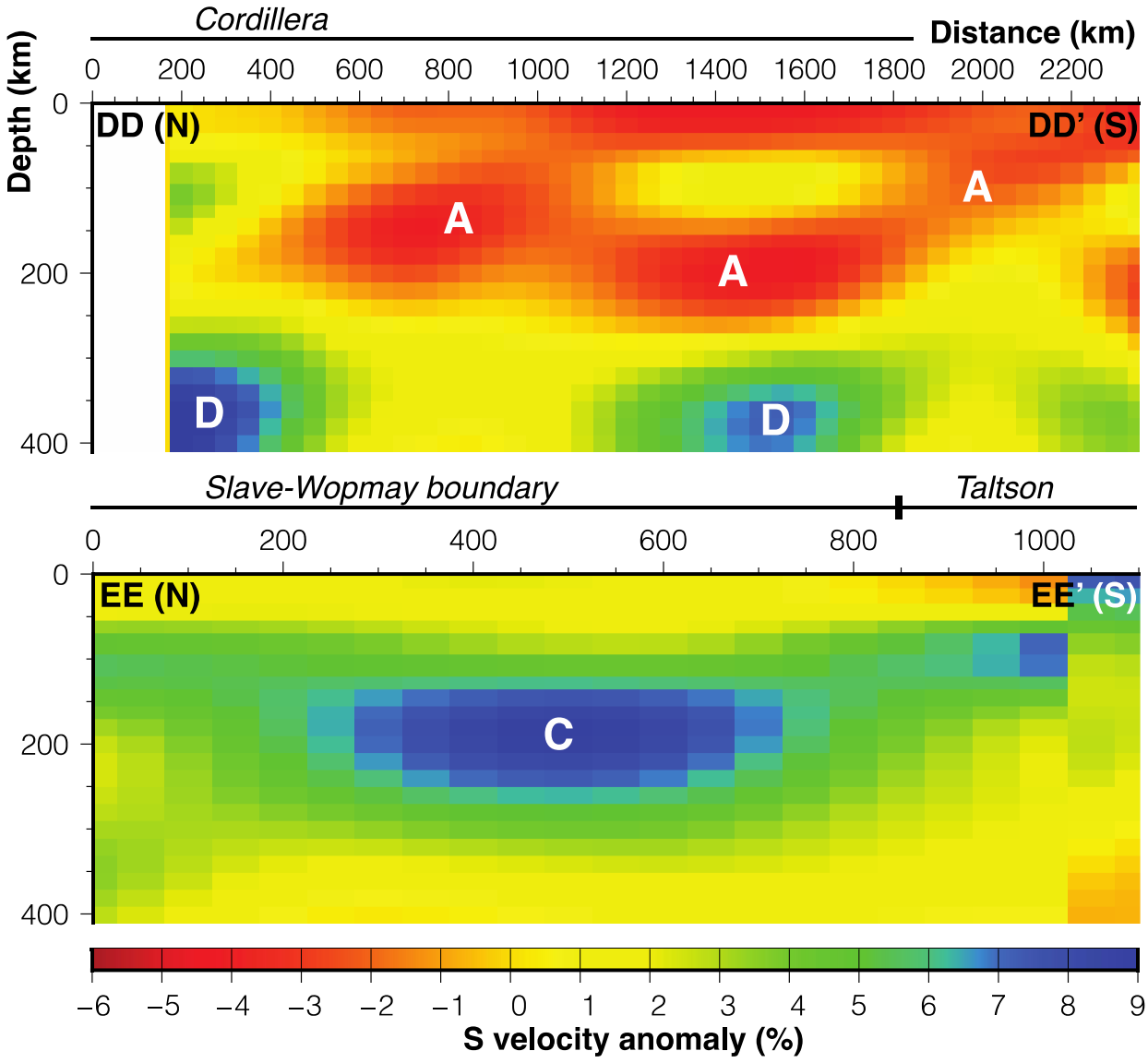

Figure 12: Additional relative-velocity cross-sections along the strike of the Cordillera (top) and across a high-velocity feature (C) near Great Slave Lake.